Journal of Southeast University (English Edition) Vol. 38, No. 4, pp. 323 − 331 Dec. 2022 ISSN 1003—7985

3D non-stationary geometry-based stochastic model for unmanned aerial vehicle air-to-ground multi-input multi-output channels

Yan Feng[1,2] Zhou Tianxiang[1] Li Hao[2] Pang Jingming[3]
Ding Kai[2] Xia Weiwei[1] Shen Lianfeng[1]

([1]National Mobile Communications Research Laboratory, Southeast University, Nanjing 210096, China)
([2]Science and Technology on Near-Surface Detection Laboratory, Wuxi 214035, China)
([3]Jiangsu Zhongli Electronic Information Sci-Tech Co., Ltd., Changshu 215542, China)

Abstract: A three-dimensional non-stationary geometry-based stochastic model for unmanned aerial vehicle (UAV) air-to-ground multi-input multi-output (MIMO) channels is proposed. The scatterers surrounding the UAV and ground station are assumed to be distributed on the surface of two cylinders in the proposed model. The impact of UAV rotations and accelerated motion is considered to describe channel non-stationarity. The computational methods of the corresponding time-variant parameters, such as UAV antenna array angles, time delays, and maximum Doppler frequencies, are theoretically deduced. The model is then used to derive channel statistical properties such as space-time correlation functions and Doppler power spectral density. Finally, numerical simulations are run to validate the channel's statistical properties. The simulation results show that increasing the UAV and ground station accelerations can reduce the time correlation function and increase channel non-stationarity in the time domain. Furthermore, the UAV's rotation significantly influences the spatial correlation function, with rolling having a greater influence than pitching. Similarly, the different directions of UAV movement significantly impact the Doppler power spectral density.

Key words: unmanned aerial vehicles (UAVs); geometry-based stochastic model (GBSM); air-to-ground channels
DOI: 10.3969/j.issn.1003 − 7985.2022.04.001

Unmanned aerial vehicle (UAV) communications have recently been widely used in civil and military applications[1], such as disaster relief, emergency assistance, and environmental monitoring[2]. Channel modeling is a critical issue in these applications. Thus, developing reliable and accurate UAV channel models is critical to provide theoretical support for designing UAV communication systems.

Many related works on UAV air-to-ground channel modeling have been published. UAV air-to-ground (A2G) channel models can be broadly classified into deterministic and stochastic models using the methods described in Refs. [3 − 4]. Deterministic models assume that the scatterer distributions in the environment are fixed; hence, the performance of communication systems can be estimated using electromagnetic wave propagation theory. There are three types of deterministic models: computational electromagnetic (CEM) models, empirical models, and theoretical models. The key methods of CEM models include finite-difference-time-domain and ray tracing. For example, the authors of Ref. [5] proposed a novel spatial partitioning ray tracing algorithm for tracking the propagation path of electromagnetic waves on the sea surface. They modeled the sea surface channel and compared the simulation results to realistic measurement data, which confirmed the model's accuracy. Deterministic channel modeling, however, is highly dependent on channel environments and has a high level of complexity.

Stochastic models assume that scatterers are not distributed in fixed locations but according to a statistical law. Stochastic models not only provide acceptable accuracy but also reduce modeling complexity. Non-geometry-based stochastic models (NGSMs) and geometry-based stochastic models (GBSMs) are two types of stochastic models (GBSMs). NGSMs rely heavily on channel measurements, but they cannot accurately characterize minor channel environment changes. The authors of Ref. [6] modeled the channel using an improved tapped delay filter model with time-variant coefficients and observed the power delay distribution and Doppler shift characteristics. GBSMs typically assume that scatterers are distributed on geometric surfaces that lack realistic measurements, such as spheres, ellipsoids, and cylinders. The authors of Ref. [7] proposed a single-sphere model for three-dimensional (3D) narrowband multi-user MIMO channels, with scatterers distributed on the surface of the sphere around the ground station (GS). The ellipsoid

Received 2022-05-17, **Revised** 2022-10-30.

Biography: Yan Feng (1983—), male, doctor, associate professor, feng.yan@seu.edu.cn.

Foundation items: The Pre-Research Fund of Science and Technology on Near-Surface Detection Laboratory (No. 6142414190405, 6142414200505), the Specialized Development Foundation for the Achievement Transformation of Jiangsu Province (No. BA2019025).

Citation: Yan Feng, Zhou Tianxiang, Li Hao, et al. 3D non-stationary geometry-based stochastic model for unmanned aerial vehicle air-to-ground multi-input multi-output channels[J]. Journal of Southeast University (English Edition), 2022, 38(4): 323 − 331. DOI: 10.3969/j.issn.1003 − 7985.2022.04.001.

model was used in Ref. [8] to describe the scatterer distribution. The UAV and GS were assumed to be located on the focal points of an ellipsoid. The cylinder model was used to describe the scatterer distribution around the GS, whereas the UAV is free of scatterers in Refs. [9 – 11].

Furthermore, channel stationarity is an essential consideration in UAV channel modeling. Non-stationarity can be ascribed to various factors, including UAV motion and rotation. On the one hand, while the UAV may move at high velocities in realistic scenarios, channels can only be considered stationary at very short intervals. The UAV motion could have a significant impact on channel performance. On the other hand, wind and atmospheric pressure can trigger UAV rotation, causing the UAV antennas to swing randomly. The authors of Ref. [12] investigated the non-stationarities of channels caused by UAV motion. Ref. [13] considered both UAV and GS mobilities, but only non-line-of-sight components and single bounces around GS were considered in the channel models. Furthermore, these previous works did not consider the rotation of the UAV caused by wind and atmospheric pressure. The authors of Ref. [14] considered the impact of both time-variant antenna orientation angles and elevation angles generated by UAV rotation.

However, they did not investigate the effect of UAV accelerated motion on channel properties. Furthermore, they failed to account for both UAV rotation and accelerated motion. To fill these gaps, the non-stationary UAV A2G channel model based on two-cylinder GBSMs is investigated, which can describe the scatterer distribution around the transmitter. Furthermore, the proposed model considers both the accelerated motion and rotations of the UAV. The main contributions are summarized below. 1) We propose a two-cylinder-based 3D GBSM for non-stationary air-to-ground multi-input multi-output (MIMO) channels for UAVs, taking scattering around the UAV into account. To more accurately characterize channel non-stationarities, the proposed model considers the impact of UAV accelerated motions and rotations simultaneously. 2) We theoretically derive the random transmitter antenna array angles caused by UAV rotation, time-variant time delays, and maximum Doppler frequency. The statistical properties of the channel, such as space-time correlation functions and Doppler power spectral density, are also deduced. 3) Finally, numerical simulations are conducted to validate the impacts of UAV accelerated motions and rotations on the statistical properties.

1 Proposed 3D UAV A2G MIMO GBSM

Herein, a UAV MIMO communication system is designed. The UAV is equipped with M_T antennas, while the GS is equipped with M_R antennas. Without compromising generalizability, we assume $M_T = M_R = 2$. δ_T and δ_R are the antenna spacing at the UAV and GS, respectively. The proposed model is depicted in Fig. 1, where the two cylinders are located around the UAV and GS, respectively, and the corresponding effective scatterers are distributed on the surfaces of the two cylinders. Following the model in Refs. [15 – 17], the two-cylinder model is used because in real scenarios, such as urban

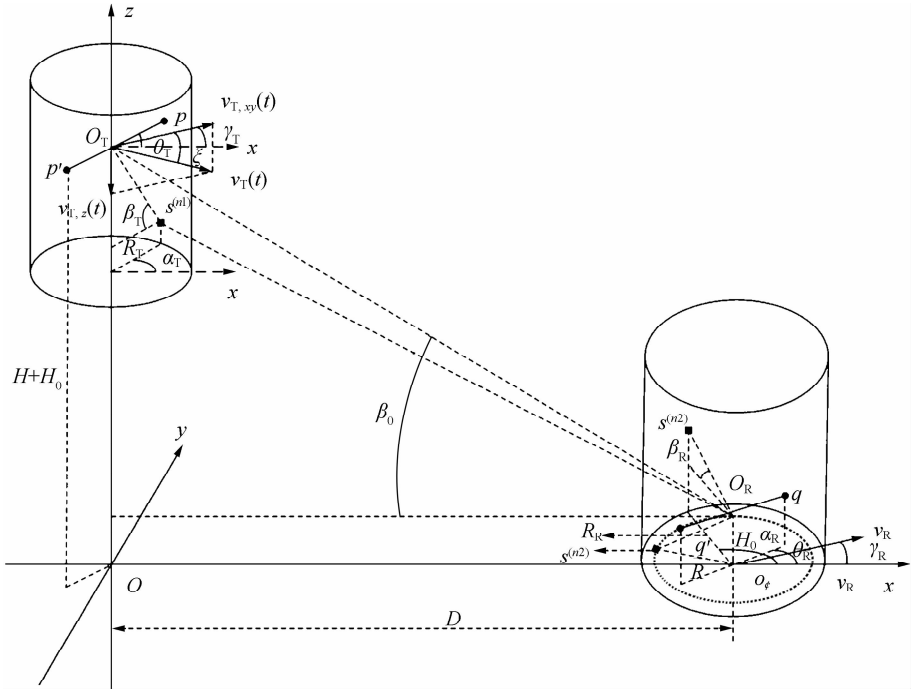

Fig. 1 The proposed GBSM for UAV air-to-ground MIMO channels

scenarios, obstacles near UAVs at low altitudes may cause scattering. Thus, the scattering around the UAV must be considered, the distribution of which can be described by the cylinder located around the UAV. We assume there are N_1 effective scatterers around the UAV, distributed on the surface of a cylinder with radius R_T, with the n_1-th ($n_1 = 1, 2, \ldots, N_1$) scatterer denoted as $s^{(n_1)}$. Similarly, there are N_2 effective scatterers on the surface of a cylinder with radius R_R, with the n_2-th ($n_2 = 1, 2, \ldots, N_2$) effective scatterer denoted as $s^{(n_2)}$. N_3 effective scatterers represent the ground reflection on the bottom surface of a cylinder with a radius $0 \leqslant R \leqslant R_R$. The n_3-th ($n_3 = 1, 2, \ldots, N_3$) effective scatterer is represented by $s^{(n_3)}$. Received signals contain five components: line-of-sight (LoS) components (the signal from the p-th antenna of the transmitter to the q-th antenna of the receiver, i. e., $T_p \rightarrow R_q$), SB-U components (the signal from the p-th antenna of the transmitter to the q-th antenna of the receiver through the scatterers around the UAV, i. e., $T_p \rightarrow s^{(n_1)} \rightarrow R_q$), SB-G components (the signal from the p-th antenna of the transmitter to the q-th antenna of the receiver through the scatterers around the GS, i. e., $T_p \rightarrow s^{(n_2)} \rightarrow R_q$), SB-GR components (the signal from the p-th antenna of the transmitter to the q-th antenna of the receiver through the scatterers on the ground, i. e., $T_p \rightarrow s^{(n_3)} \rightarrow R_q$), DB components (the signal from the pth antenna of the transmitter to the q-th antenna of the receiver through both the scatterers around the UAV and GS, i. e., $T_p \rightarrow s^{(n_1)} \rightarrow s^{(n_2)} \rightarrow R_q$). The height of GS is denoted by H_0. The horizontal and vertical distances between the UAV and the GS at time $t = 0$ s are denoted by D and H, respectively, which satisfy $D \gg R_{T/R}$.

Furthermore, both the UAV and the GS are assumed to move in uniformly accelerated motion with time-variant velocities $v_T(t)$ and $v_R(t)$, respectively. $v_T(t)$ can be decomposed into a horizontal component $v_{T,xy}(t)$ and a vertical component $v_{T,z}(t)$. Then we define $\langle v_{T,xy}(t), v_T(t) \rangle = \xi$, $\langle v_{T,xy}(t), +x \rangle = \gamma_T$, where $\langle \cdot, \cdot \rangle$ denotes included angles. The transceivers do not change directions during the movement. The angle pair ξ and γ_T are used to describe UAV movement in 3D space. The angle γ_R denotes the GS moving direction in the x-y plane.

The non-stationarity of the channel is primarily caused by transceiver mobility and UAV rotation. Because the UAV and GS move in uniformly accelerated motion, the propagation time delays, and maximum Doppler frequency are time-variant. In real-world scenarios, scatterers exist at random throughout the environment. When the UAV moves, the scatterers around it change as well. Angles of the scatterers can be expressed statistically by the same distribution. $\alpha_T^{(n_1)}$ and $\beta_T^{(n_1)}$ are defined as the angles of departure (AODs) of waves impinging on the effective scatterers $s^{(n_1)}$. $\alpha_R^{(n_1)}$ and $\beta_R^{(n_1)}$ are defined as the angles of arrival (AOAs) of waves from the effective scatterers $s^{(n_1)}$ to the receiver. We use $\alpha_T^{LoS}, \beta_T^{LoS}, \alpha_R^{LoS}$, and β_R^{LoS} to denote the AOD and AOA of LoS components. They are not shown in Fig. 1 for brevity.

Second, in realistic scenarios, the UAV rotation may be caused by wind and atmospheric pressure, causing the UAV antennas to swing randomly, resulting in the unpredictability of the orientation angle and elevation angle of the UAV antenna arrays. As shown in Fig. 2, the proposed model considers the effects of UAV rotation, such as rolling, pitching, and heaving. Rolling operations refer to the movement of UAV antennas between the x- and z-axes, pitching operations refer to the movement of UAV antennas between the y- and z-axes, and heaving operations refer to the movement of UAV antennas up and down the z-axis. $\psi_T(t)$ and $\theta_T(t)$ are the elevation and orientation angles of the UAV antenna arrays, respectively. As the UAV heaves along the z-axis, heaving operations are assumed to be included in the UAV vertical movement for simplicity. Therefore, the proposed model focuses on the UAV's rolling and pitching operations. θ_R denotes the constant azimuth angle of the GS antenna array.

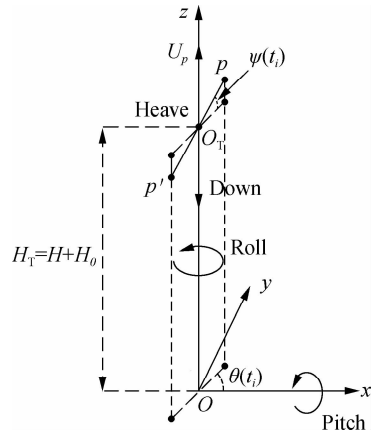

Fig. 2 The rotation of UAV

The carrier frequency is f_c, and the received complex fading envelope signal between the UAV's p-th antenna and the GS's q-th antenna is a superstition of LoS, SB-U, SB-G, SB-GR, and DB components. The received complex envelope signal is denoted as

$$h_{pq}(t) = h_{pq}^{LoS}(t) + h_{pq}^{SB\text{-}U}(t) + h_{pq}^{SB\text{-}G}(t) + h_{pq}^{SB\text{-}GR}(t) + h_{pq}^{DB}(t) \tag{1}$$

where multi-path components can be expressed as follows:

$$h_{pq}^{LoS}(t) = \sqrt{\frac{K\Omega_{pq}}{K+1}} e^{-j2\pi f_c \tau_{pq}(t)} e^{j2\pi f_{Rm}(t)t[\cos(\alpha_R^{LoS}-\gamma_R)\cos\beta_R^{LoS}]} \cdot e^{j2\pi f_{Tm}(t)t[\cos(\alpha_T^{LoS}-\gamma_T)\cos\beta_T^{LoS}\cos\xi+\sin\beta_T^{LoS}\sin\xi]} \tag{2}$$

$$h_{pq}^{SB\text{-}U}(t) = \sqrt{\frac{\eta_{SB\text{-}U}\Omega_{pq}}{K+1}} \lim_{N_1\to\infty} \frac{1}{\sqrt{N_1}} \sum_{n_1=1}^{N_1} e^{j\varphi^{(n_1)}} e^{-j2\pi f_c \tau_{pq,n}(t)} \cdot$$

$$\mathrm{e}^{\mathrm{j}2\pi f_{\mathrm{Tm}}(t)t[\cos(\alpha_{\mathrm{T}}^{(n_1)}-\gamma_{\mathrm{T}})\cos\beta_{\mathrm{T}}^{(n_1)}\cos\xi+\sin\beta_{\mathrm{T}}^{(n_1)}\sin\xi]}\cdot \mathrm{e}^{\mathrm{j}2\pi f_{\mathrm{Rm}}(t)t[\cos(\alpha_{\mathrm{R}}^{(n_1)}-\gamma_{\mathrm{R}})\cos\beta_{\mathrm{R}}^{(n_1)}]} \tag{3}$$

$$h_{pq}^{\mathrm{SB\text{-}G}}(t)=\sqrt{\frac{\eta_{\mathrm{SB\text{-}G}}\Omega_{pq}}{K+1}}\lim_{N_2\to\infty}\frac{1}{\sqrt{N_2}}\sum_{n_2=1}^{N_2}\mathrm{e}^{\mathrm{j}\varphi^{(n_2)}}\mathrm{e}^{-\mathrm{j}2\pi f_c\tau_{pq,n_2}(t)}\cdot \mathrm{e}^{\mathrm{j}2\pi f_{\mathrm{Tm}}(t)t[\cos(\alpha_{\mathrm{T}}^{(n_2)}-\gamma_{\mathrm{T}})\cos\beta_{\mathrm{T}}^{(n_2)}\cos\xi+\sin\beta_{\mathrm{T}}^{(n_2)}\sin\xi]}\cdot \mathrm{e}^{\mathrm{j}2\pi f_{\mathrm{Rm}}(t)t[\cos(\alpha_{\mathrm{R}}^{(n_2)}-\gamma_{\mathrm{R}})\cos\beta_{\mathrm{R}}^{(n_2)}]} \tag{4}$$

$$h_{pq}^{\mathrm{SB\text{-}GR}}(t)=\sqrt{\frac{\eta_{\mathrm{SB\text{-}GR}}\Omega_{pq}}{K+1}}\lim_{N_3\to\infty}\frac{1}{\sqrt{N_3}}\sum_{n_3=1}^{N_3}\mathrm{e}^{\mathrm{j}\varphi^{(n_3)}}\mathrm{e}^{-\mathrm{j}2\pi f_c\tau_{pq,n_3}(t)}\cdot \mathrm{e}^{\mathrm{j}2\pi f_{\mathrm{Tm}}(t)t[\cos(\alpha_{\mathrm{T}}^{(n_3)}-\gamma_{\mathrm{T}})\cos\beta_{\mathrm{T}}^{(n_3)}\cos\xi+\sin\beta_{\mathrm{T}}^{(n_3)}\sin\xi]}\cdot \mathrm{e}^{\mathrm{j}2\pi f_{\mathrm{Rm}}(t)t[\cos(\alpha_{\mathrm{R}}^{(n_3)}-\gamma_{\mathrm{R}})\cos\beta_{\mathrm{R}}^{(n_3)}]} \tag{5}$$

$$h_{pq}^{\mathrm{DB}}(t)=\sqrt{\frac{\eta_{\mathrm{DB}}\Omega_{pq}}{K+1}}\lim_{N_1,N_2\to\infty}\frac{1}{\sqrt{N_1N_2}}\sum_{n_1,n_2=1}^{N_1,N_2}\mathrm{e}^{\mathrm{j}\varphi^{(n_1,n_2)}}\mathrm{e}^{-\mathrm{j}2\pi f_c\tau_{pq,n_1,n_2}(t)}\cdot \mathrm{e}^{\mathrm{j}2\pi f_{\mathrm{Tm}}(t)t[\cos(\alpha_{\mathrm{T}}^{(n_1)}-\gamma_{\mathrm{T}})\cos\beta_{\mathrm{T}}^{(n_1)}\cos\xi+\sin\beta_{\mathrm{T}}^{(n_1)}\sin\xi]}\cdot \mathrm{e}^{\mathrm{j}2\pi f_{\mathrm{Rm}}(t)t[\cos(\alpha_{\mathrm{R}}^{(n_1)}-\gamma_{\mathrm{R}})\cos\beta_{\mathrm{R}}^{(n_1)}]} \tag{6}$$

where $\tau_{pq}(t)=\varepsilon_{pq}(t)/c$, $\tau_{pq,n_1}(t)=[\varepsilon_{pn_1}(t)+\varepsilon_{n_1q}(t)]/c$, $\tau_{pq,n_2}(t)=[\varepsilon_{pn_2}(t)+\varepsilon_{n_2q}(t)]/c$, $\tau_{pq,n_3}(t)=[\varepsilon_{pn_3}(t)+\varepsilon_{n_3q}(t)]/c$, $\tau_{pq,n_1,n_2}(t)=[\varepsilon_{pn_1}(t)+\varepsilon_{n_1n_2}(t)+\varepsilon_{n_2q}(t)]/c$, which represent the propagation time delays of the waves through links $T_p\to R_q$, $T_p\to s^{(n_1)}\to R_q$, $T_p\to s^{(n_2)}\to R_q$, $T_p\to s^{(n_3)}\to R_q$ and $T_p\to s^{(n_1)}\to s^{(n_2)}\to R_q$. $\varepsilon_{pq}(t)$, $\varepsilon_{pn_1}(t)$, $\varepsilon_{n_1q}(t)$, $\varepsilon_{pn_2}(t)$, $\varepsilon_{n_2q}(t)$, $\varepsilon_{pn_3}(t)$, $\varepsilon_{n_3q}(t)$ and $\varepsilon_{n_1n_2}(t)$ denote the distances of corresponding links respectively, and c denotes the speed of light. Ω_{pq} and K denote the total power received and the Rician factor, respectively. In addition, $\eta_{\mathrm{SB\text{-}U}}$, $\eta_{\mathrm{SB\text{-}G}}$, $\eta_{\mathrm{SB\text{-}GR}}$, and η_{DB} are energy-related parameters, which refer to the ratios of corresponding reflections to the total scattering power $\Omega_{pq}/(K_{pq}+1)$ and satisfy $\eta_{\mathrm{SB\text{-}U}}+\eta_{\mathrm{SB\text{-}G}}+\eta_{\mathrm{SB\text{-}GR}}+\eta_{\mathrm{DB}}=1$. The phases caused by scattering are expressed as $\varphi^{(n_1)}$, $\varphi^{(n_2)}$, $\varphi^{(n_3)}$, and $\varphi^{(n_1,n_2)}$, which are independent random variables and distributed uniformly over $[-\pi,\pi)$. $f_{\mathrm{Tm}}=v_{\mathrm{T}}(t)/\lambda$ and $f_{\mathrm{Rm}}=v_{\mathrm{R}}(t)/\lambda$ denote the time-variant maximum Doppler frequencies of the UAV and GS, respectively.

The proposed model assumes that N_1, N_2, and $N_3\to\infty$, so continuous variables α_{T}, β_{T}, α_{R}, β_{R} can be used to replace discrete variables $\alpha_{\mathrm{T}}^{(n_i)}$, $\beta_{\mathrm{T}}^{(n_i)}$, $\alpha_{\mathrm{R}}^{(n_i)}$ and $\beta_{\mathrm{R}}^{(n_i)}$. Furthermore, it is assumed the azimuth and elevation angles are independent. Finally, the joint probability density function (PDF) $f(\alpha,\beta)$ can be approximated as the product of margin PDFs, i.e., $f(\alpha)$ and $f(\beta)$.

The Von-Mises PDF[10] is applied to describe the azimuth angles α_{T} and α_{R}, which are defined as follows:

$$f(\alpha)=\frac{\mathrm{e}^{k}\cos(\alpha-\alpha_\mu)}{2\pi I_0(k)}\qquad -\pi<\alpha\leqslant\pi \tag{7}$$

where $I_0(\cdot)$ denotes the zeroth-order modified Bessel function of the first kind; $\alpha_\mu\in[-\pi,\pi]$ denotes the mean value of α. The angle spread around the mean angle is controlled by the parameter k, and as k increases, the scattering becomes more nonisotropic.

The cosine PDF[18] is used to describe the elevation angles β_{T} and β_{R}, which can be expressed as

$$f(\beta)=\frac{\pi}{4\beta_{\mathrm{m}}}\cos\left(\frac{\pi}{2}\frac{\beta-\beta_\mu}{\beta_{\mathrm{m}}}\right)\qquad |\beta-\beta_\mu|\leqslant\beta_{\mathrm{m}}\leqslant\frac{\pi}{2} \tag{8}$$

noting that $\beta\in[\beta_\mu-\beta_{\mathrm{m}},\beta_\mu+\beta_{\mathrm{m}}]$, β_{m}, and β_μ denote the maximum and mean angles, respectively. Here we use $\beta_\mu-\beta_{\mathrm{m}}=\beta_1$ and $\beta_\mu+\beta_{\mathrm{m}}=\beta_2$, therefore $\beta\in[\beta_1,\beta_2]$.

2 Statistical Properties

2.1 Distribution of random UAV antenna array angles

A Gauss-Markov process of temporal relation[11] is used to describe the UAV rotation. The antenna array orientation angle ψ_{T} and elevation angle θ_{T} can be expressed as

$$\psi_{\mathrm{T}}(t_i)=\rho_\psi^i\psi_{\mathrm{T}}(t_0)+(1-\rho_\psi^i)\mu_{\psi_{\mathrm{T}}}+\sqrt{1-\rho_\psi^2}\sum_{j=0}^{i-1}\rho_\psi^{i-j-1}X_j \tag{9}$$

$$\theta_{\mathrm{T}}(t_i)=\rho_\theta^i\theta_{\mathrm{T}}(t_0)+(1-\rho_\theta^i)\mu_{\theta_{\mathrm{T}}}+\sqrt{1-\rho_\theta^2}\sum_{j=0}^{i-1}\rho_\theta^{i-j-1}Y_j \tag{10}$$

where $i=1,2,3,\cdots$; $\psi_{\mathrm{T}}(t_0)$ and $\theta_{\mathrm{T}}(t_0)$ denote the angles at time $t=0$; $\psi_{\mathrm{T}}(t_i)$ and $\theta_{\mathrm{T}}(t_i)$ denote the angles at time $t_i=it_{\mathrm{step}}$, t_{step} is the time step; $\mu_{\psi\mathrm{T}}$ and $\mu_{\theta\mathrm{T}}$ are constants representing the mean elevation and orientation angle of the transmitter antenna array; $\rho_{\psi/\theta}$ denotes two tuning values within range $[0,1]$; X and Y are random variables following the Gaussian distribution.

2.2 Time-variant delays

The transceiver and scatterer coordinates change over time, resulting in time-varying delays and maximum Doppler frequencies. The transceiver's velocity can be expressed as

$$v_{\mathrm{T}}(t)=v_{\mathrm{T}}(t_0)+a_{\mathrm{T}}t \tag{11}$$

$$v_{\mathrm{R}}(t)=v_{\mathrm{R}}(t_0)+a_{\mathrm{R}}t \tag{12}$$

where $a_{\mathrm{T/R}}$ is the acceleration.

After time t, the displacements of the transceivers can be expressed as

$$\Delta S_{\mathrm{T}}(t)=\frac{1}{2}a_{\mathrm{T}}t^2+v_{\mathrm{T}}(t_0)t \tag{13}$$

$$\Delta S_{\mathrm{R}}(t)=\frac{1}{2}a_{\mathrm{R}}t^2+v_{\mathrm{R}}(t_0)t \tag{14}$$

where $D_{x/y/z}^{n_i}$ denotes the scatterer coordinates $s^{(n_i)}$ along the $x/y/z$ axis; $D_{x/y/z}^{\mathrm{T}}(t)$ and $D_{x/y/z}^{\mathrm{R}}(t)$ denote the UAV and GS coordinates, respectively. They are time variants

but abbreviated as $D_{x/y/z}$ for simplicity. Based on the spatial distance formula, distances between the scatterers and antennas can be easily expressed as follows:

$$\varepsilon_{pq} = \sqrt{(D_x^{\mathrm{T}}(t) - D_x^{\mathrm{R}}(t))^2 + (D_y^{\mathrm{T}}(t) - \mathrm{D}_y^{R}(t))^2 + (D_z^{\mathrm{T}}(t) - D_z^{\mathrm{R}}(t))^2} \tag{15}$$

$$\varepsilon_{pn_i} = \sqrt{(D_x^{\mathrm{T}}(t) - D_x^{n_i}(t))^2 + (D_y^{\mathrm{T}}(t) - D_y^{n_i}(t))^2 + (D_z^{\mathrm{T}}(t) - D_z^{n_i}(t))^2} \tag{16}$$

$$\varepsilon_{n_iq} = \sqrt{(D_x^{n_i}(t) - D_x^{\mathrm{R}}(t))^2 + (D_y^{n_i}(t) - D_y^{\mathrm{R}}(t))^2 + (D_z^{n_i}(t) - D_z^{\mathrm{R}}(t))^2} \tag{17}$$

where $i = 1, 2, 3$ denotes the three different scatterers. Therefore, the 3D coordinates of the UAV, GS, and scatterers can be expressed as follows. Due to space constraints, only the transmitter and receiver coordinates are provided.

$$D_x^{\mathrm{T}}(t) = \Delta S_{\mathrm{T}}(t)\cos\xi\cos\gamma_{\mathrm{T}} + \Delta_{\mathrm{T}}\cos\psi_{\mathrm{T}}(t)\cos\theta_{\mathrm{T}}(t) \tag{18a}$$

$$D_y^{\mathrm{T}}(t) = \Delta S_{\mathrm{T}}(t)\cos\xi\sin\gamma_{\mathrm{T}} + \Delta_{\mathrm{T}}\cos\psi_{\mathrm{T}}(t)\sin\theta_{\mathrm{T}}(t) \tag{18b}$$

$$D_z^{\mathrm{T}}(t) = -\Delta S_{\mathrm{T}}(t)\sin\xi + \Delta_{\mathrm{T}}\sin\psi_{\mathrm{T}}(t) + D\tan\beta_0 + H_0 \tag{18c}$$

$$D_x^{\mathrm{R}}(t) = \Delta S_{\mathrm{R}}(\mathrm{t})\cos\gamma_{\mathrm{R}} + \Delta_{\mathrm{R}}\cos\psi_{\mathrm{R}}\cos\theta_{\mathrm{R}} + D \tag{19a}$$

$$D_y^{\mathrm{R}}(t) = \Delta S_{\mathrm{R}}(t)\sin\gamma_{\mathrm{R}} + \Delta_{\mathrm{R}}\cos\psi_{\mathrm{R}}\sin\theta_{\mathrm{R}} \tag{19b}$$

$$D_z^{\mathrm{R}}(t) = \Delta_{\mathrm{R}}\sin\psi_{\mathrm{R}} + H_0 \tag{19c}$$

where Δ_{T} denotes the distance between the p-th UAV antenna and the midpoint of the antenna array; Δ_{R} denotes the distance between the q-th GS antenna and the midpoint of the antenna array. For uniform linear antenna arrays, these parameters can be expressed as

$$\Delta_{\mathrm{T}} = \frac{1}{2}(M_{\mathrm{T}} + 1 - 2p)\delta_{\mathrm{T}} \tag{20}$$

$$\Delta_{\mathrm{R}} = \frac{1}{2}(M_{\mathrm{R}} + 1 - 2q)\delta_{\mathrm{R}} \tag{21}$$

2.3 Time-variant maximum Doppler frequencies

The transceivers are assumed to maintain uniformly accelerated motion, resulting in time-variant maximum Doppler frequencies. The expressions are as follows:

$$f_{\mathrm{Tm}}(t) = \frac{v_{\mathrm{T}}(t)}{\lambda} = \frac{v_{\mathrm{T}}(t_0)}{\lambda} + \frac{a_{\mathrm{T}}}{\lambda}t \tag{22}$$

$$f_{\mathrm{Rm}}(t) = \frac{v_{\mathrm{R}}(t)}{\lambda} = \frac{v_{\mathrm{R}}(t_0)}{\lambda} + \frac{a_{\mathrm{R}}}{\lambda}t \tag{23}$$

2.4 Space-time correlation function

For two random complex fading envelopes $h_{pq}(t)$ and $h_{p'q'}(t)$, the normalized space-time correlation function is defined as

$$R_{pq,p'q'}(\delta_{\mathrm{T}},\delta_{\mathrm{R}},t,\tau) = \frac{E[h_{pq}(t)h_{p'q'}^{*}(t-\tau)]}{\sqrt{E[|h_{pq}(t)|^2]E[|h_{p'q'}(t)|^2]}} \tag{24}$$

where $(\cdot)^*$ denotes the complex conjugate operation and $E[\cdot]$ denotes the statistical expectation operator.

Eq. (24) is a function of timet, time delay τ, and antenna spacings δ_{T} and δ_{R}. For simplicity, it is assumed that each component is independent of the others, whereas some components may be related in realistic scenarios, which is the subject of future work. Thus, the correlation function expression can be decomposed into five components:

$$\begin{aligned} R_{pq,p'q'}(\delta_{\mathrm{T}},\delta_{\mathrm{R}},t,\tau) = {} & R_{pq,p'q'}^{\mathrm{LoS}}(\delta_{\mathrm{T}},\delta_{\mathrm{R}},t,\tau) + \\ & R_{pq,p'q'}^{\mathrm{SB\text{-}U}}(\delta_{\mathrm{T}},\delta_{\mathrm{R}},t,\tau) + R_{pq,p'q'}^{\mathrm{SB\text{-}G}}(\delta_{\mathrm{T}},\delta_{\mathrm{R}},t,\tau) + \\ & R_{pq,p'q'}^{\mathrm{SB\text{-}GR}}(\delta_{\mathrm{T}},\delta_{\mathrm{R}},t,\tau) + R_{pq,p'q'}^{\mathrm{DB}}(\delta_{\mathrm{T}},\delta_{\mathrm{R}},t,\tau) \end{aligned} \tag{25}$$

Substituting Eq. (2) into Eq. (24), the space-time correlation function of the SB-U components can be expressed as

$$\begin{aligned} R_{pq,p'q'}^{\mathrm{SB\text{-}U}}(\delta_{\mathrm{T}},\delta_{\mathrm{R}},t,\tau) = {} & \frac{\eta_{\mathrm{SB\text{-}U}}}{K+1}\int_{\beta_{\mathrm{T1}}}^{\beta_{\mathrm{T2}}}\int_{-\pi}^{\pi} \mathrm{e}^{-\mathrm{j}\frac{2\pi}{\lambda}[\varepsilon_{pq,n}(t)-\varepsilon_{p'q',n}(t-\tau)]} \cdot \\ & \mathrm{e}^{\mathrm{j}2\pi f_{\mathrm{Tm}}(t)tA_{\mathrm{T}}}\mathrm{e}^{\mathrm{j}2\pi f_{\mathrm{Rm}}(t)tA_{\mathrm{R}}}\mathrm{e}^{-\mathrm{j}2\pi f_{\mathrm{Tm}}(t-\tau)(t-\tau)A_{\mathrm{T}}(t-\tau)} \\ & \mathrm{e}^{-\mathrm{j}2\pi f_{\mathrm{Rm}}(t-\tau)(t-\tau)A_{\mathrm{R}}(t-\tau)}f(\alpha_{\mathrm{T}})f(\beta_{\mathrm{T}})\,\mathrm{d}\alpha_{\mathrm{T}}\mathrm{d}\beta_{\mathrm{T}} \end{aligned} \tag{26}$$

where $A_{\mathrm{T}}(\alpha_{\mathrm{T}},\beta_{\mathrm{T}}) = \cos(\alpha_{\mathrm{T}} - \gamma_{\mathrm{T}})\cos\beta_{\mathrm{T}}\cos\xi + \sin\beta_{\mathrm{T}}\sin\xi$, $A_{\mathrm{R}}(\alpha_{\mathrm{R}},\beta_{\mathrm{R}}) = \cos(\alpha_{\mathrm{R}} - \gamma_{\mathrm{R}})\cos\beta_{\mathrm{R}}$ for simplicity. Similarly, correlation function expressions for LoS, SB-G, SB-GR, and DB components can be expressed as

$$\begin{aligned} R_{pq,p'q'}^{\mathrm{SB\text{-}G}}(\delta_{\mathrm{T}},\delta_{\mathrm{R}},t,\tau) = {} & \frac{\eta_{\mathrm{SB\text{-}G}}}{K+1}\int_{\beta_{\mathrm{R1}}}^{\beta_{\mathrm{R2}}}\int_{-\pi}^{\pi} \mathrm{e}^{-\mathrm{j}\frac{2\pi}{\lambda}[\varepsilon_{pq,n}(t)-\varepsilon_{p'q',n}(t-\tau)]} \cdot \\ & \mathrm{e}^{\mathrm{j}2\pi f_{\mathrm{Tm}}tA_{\mathrm{T}}(t)}\mathrm{e}^{\mathrm{j}2\pi f_{\mathrm{Rm}}tA_{\mathrm{R}}(t)}\mathrm{e}^{-\mathrm{j}2\pi f_{\mathrm{Tm}}(t-\tau)A_{\mathrm{T}}(t-\tau)} \cdot \\ & \mathrm{e}^{-\mathrm{j}2\pi f_{\mathrm{Rm}}(t-\tau)A_{\mathrm{R}}(t-\tau)}f(\alpha_{\mathrm{R}})f(\beta_{\mathrm{R}})\,\mathrm{d}\alpha_{\mathrm{R}}\mathrm{d}\beta_{\mathrm{R}} \end{aligned} \tag{27}$$

$$\begin{aligned} R_{pq,p'q'}^{\mathrm{SB\text{-}GR}}(\delta_{\mathrm{T}},\delta_{\mathrm{R}},t,\tau) = {} & \frac{\eta_{\mathrm{SB\text{-}GR}}}{K+1}\int_{0}^{R_{\mathrm{k}}}\int_{-\pi}^{\pi} \mathrm{e}^{-\mathrm{j}\frac{2\pi}{\lambda}[\varepsilon_{pq,n}(t)-\varepsilon_{p'q',n}(t-\tau)]} \cdot \\ & \mathrm{e}^{\mathrm{j}2\pi f_{\mathrm{Tm}}tA_{\mathrm{T}}(t)}\mathrm{e}^{\mathrm{j}2\pi f_{\mathrm{Rm}}tA_{\mathrm{R}}(t)}\mathrm{e}^{-\mathrm{j}2\pi f_{\mathrm{Tm}}(t-\tau)A_{\mathrm{T}}(t-\tau)} \cdot \\ & \mathrm{e}^{-\mathrm{j}2\pi f_{\mathrm{Rm}}(t-\tau)A_{\mathrm{R}}(t-\tau)}f(\alpha_{\mathrm{R}})f(R)\,\mathrm{d}\alpha_{\mathrm{R}}\mathrm{d}R \end{aligned} \tag{28}$$

The SB-GR component is located on the bottom surface of the GS's cylinder, i. e., a two-dimensional space. Therefore, there is a geometric relationship between R and $\beta_{\mathrm{R}}^{(n_3)}$, which is $\tan\beta_{\mathrm{R}}^{(n_3)} = H_0/R$.

$$R_{pq,p'q'}^{\mathrm{DB}}(\delta_{\mathrm{T}},\delta_{\mathrm{R}},t,\tau)=\frac{\eta_{\mathrm{DB}}}{K+1}\int_{\beta_{\mathrm{R1}}}^{\beta_{\mathrm{R2}}}\int_{-\pi}^{\pi}\int_{\beta_{\mathrm{T1}}}^{\beta_{\mathrm{T2}}}\int_{-\pi}^{\pi}\mathrm{e}^{-\mathrm{j}\frac{2\pi}{\lambda}\left[\varepsilon_{pq,\mathrm{R},\alpha_{\mathrm{R}}}(t)-\varepsilon_{p'q',\mathrm{R},\alpha_{\mathrm{R}}}(t-\tau)\right]}\cdot \mathrm{e}^{\mathrm{j}2\pi f_{\mathrm{Tm}}tA_{\mathrm{T}}(t)}\mathrm{e}^{\mathrm{j}2\pi f_{\mathrm{Rm}}tA_{\mathrm{R}}(t)}\mathrm{e}^{-\mathrm{j}2\pi f_{\mathrm{Tm}}(t-\tau)A_{\mathrm{T}}(t-\tau)}\mathrm{e}^{-\mathrm{j}2\pi f_{\mathrm{Rm}}(t-\tau)A_{\mathrm{R}}(t-\tau)}\cdot f(\alpha_{\mathrm{T}})f(\beta_{\mathrm{T}})f(\alpha_{\mathrm{R}})f(\beta_{\mathrm{R}})\,\mathrm{d}\alpha_{\mathrm{T}}\mathrm{d}\beta_{\mathrm{T}}\mathrm{d}\alpha_{\mathrm{R}}\mathrm{d}\beta_{\mathrm{R}} \quad (29)$$

2.5 Doppler power spectral density

The corresponding Doppler power spectral density can be obtained by performing the Fourier transform of the above-mentioned space-time correlation function with respect to τ, i. e., $R_{pq}(\tau)$. It can be represented as follows:

$$S_{pq}(f_{\mathrm{D}})=\int_{-\infty}^{\infty}R_{pq}(\tau)\mathrm{e}^{-2\pi f_{\mathrm{D}}\tau}\mathrm{d}\tau \quad (30)$$

where f_{D} denotes the Doppler frequency. Similar to Eq. (25), $S_{pq}(f_{\mathrm{D}})$ can be written as

$$S_{pq}(f_{\mathrm{D}})=S_{pq}^{\mathrm{LoS}}(f_{\mathrm{D}})+S_{pq}^{\mathrm{SB\text{-}U}}(f_{\mathrm{D}})+S_{pq}^{\mathrm{SB\text{-}G}}(f_{\mathrm{D}})+S_{pq}^{\mathrm{SB\text{-}GR}}(f_{\mathrm{D}})+S_{pq}^{\mathrm{DB}}(f_{\mathrm{D}}) \quad (31)$$

3 Numerical Simulations

Without actual measurements, the effects of UAV movement and rotation on the statistical properties of the channel are investigated through numerical simulations. Per the parameter settings described in Ref. [15], the parameters presented in Tab. 1 are based on numerical simulations. The horizontal distance between the transceivers is set to a small value to maximize the effects of scattering around UAVs at low altitudes. Similarly, the velocity of GS is set to a small value to obtain the effects of UAV motion on the channel properties.

Tab. 1 Parameters for simulations

Parameter	Value
Horizontal distances between UAV and GS at $t=0$ s, D/m	100
Height of GS H_0/m	5
Elevation angle of LoS path β_0	$\pi/6$
Wavelength λ/m	0.1
Radius of the cylinder around UAV R_{T}/m	5
Radius of the cylinder around GS R_{R}/m	3
Elevation angle of UAV at $t=0$ s, $\psi_{\mathrm{T}}(t_0)$	0
Elevation angle of GS ψ_{R}	0
Azimuth angle of UAV at $t=0$ s, $\theta_{\mathrm{T}}(t_0)$	$\pi/2$
Azimuth angle of GS θ_{R}	$\pi/2$
Rician factor K	0.03
Energy-related parameter of SB-U	0.05
Energy-related parameter of SB-G	0.85
Energy-related parameter of SB-GR	0.05
Energy-related parameter of DB	0.05

The influence of UAV displacement on channel statistical properties in the time domain is depicted in Fig. 3, where time correlation functions are shown with $\beta_0=\pi/6$ at $t=0$ s and $t=2$ s, respectively. When the UAV moves directly toward the GS (along the LoS path), the time correlation function is larger than in other cases with the same delay τ, indicating that channel variation is slower and is, therefore, more stationary. In addition, the time correlation functions of $\xi=\pi/4$ are greater than those of $\xi=0$ and $\xi=\pi/2$, because $\xi=\pi/4$ is closer to β_0. This indicates that channel non-stationarity is more pronounced when the UAV moves in a direction opposite the LoS.

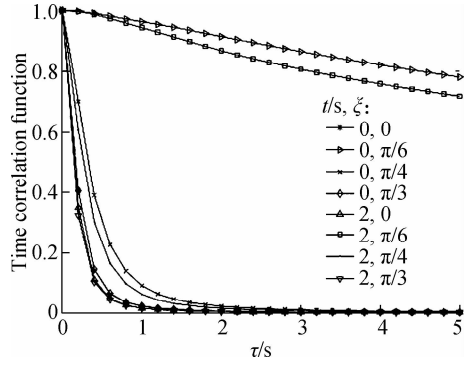

Fig. 3 Time correlation functions under UAV different directions

Fig. 4 depicts the time correlation functions for four scattering paths under varying UAV acceleration conditions. It can be observed that the time correlation functions of the four paths diminish as the time delays increase. The UAV accelerated motion significantly affects the time correlation function of SB-U and DB, as shown in Figs. 4(a) and (d). Whereas Figs. 4(b) and (c) demonstrate that the UAV's accelerated motion has a negligible effect on SB-G and SB-GR. From the perspective of SB-U and DB, the larger the UAV acceleration, the smaller the value of the time correlation function at the same τ, which indicates that the channels have lower stationarity as the UAV acceleration increases. In other words, the UAV's accelerated motion can increase the time domain non-stationarity of the channel.

Fig. 5 depicts the time correlation functions of four scattering paths under varying GS accelerations. In contrast to Fig. 4, it is evident that the GS accelerated motion significantly affects the time correlation functions of SB-G and SB-GR, as depicted in Figs. 5(b) and (c). Figs. 5 (a) and (d) demonstrate that the GS accelerated motion has almost no effect on the SB-U and DB accelerated motions. From the perspective of SB-G and SB-GR, the larger the GS acceleration, the smaller the time correlation function values at the same τ, indicating that the channels become less stationary with a large GS acceleration in the time domain.

The spatial correlation functions during pitching and rolling operations are depicted in Fig. 6. The UAV rotation angles vary randomly with time t, allowing fluctuations in the spatial correlation function. Thus, the effects

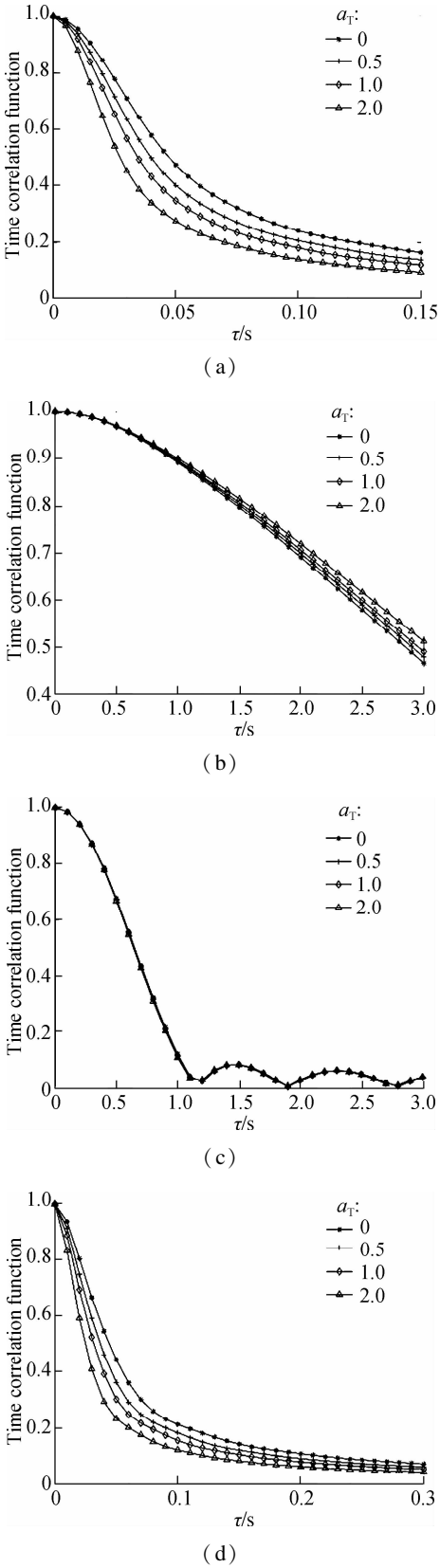

Fig. 4 Time correlation functions of UAV accelerated motion. (a) SB-U; (b) SB-G; (c) SB-GR; (d) DB

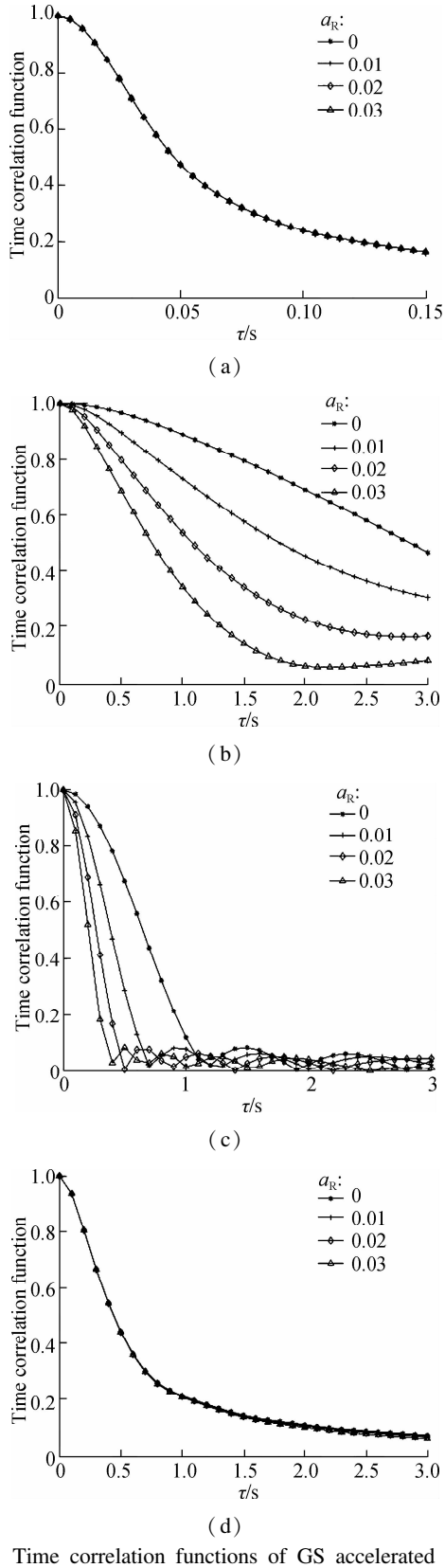

Fig. 5 Time correlation functions of GS accelerated motion. (a) SB-U; (b) SB-G; (c) SB-GR; (d) DB

of UAV rotation on the spatial correlation function can be demonstrated along the t-axis. The spatial correlation functions with rotations fluctuate with time t, whereas those without rotation decrease linearly, as shown in Fig. 6. Comparing the curves of pitching operations in Fig. 6 (a) and rolling operations in Fig. 6 (b) reveals that the spatial correlation functions with rolling fluctuate more

dramatically than those with pitching, indicating that the influence of rolling operations on the channel's statistical properties is greater than that of pitching operations.

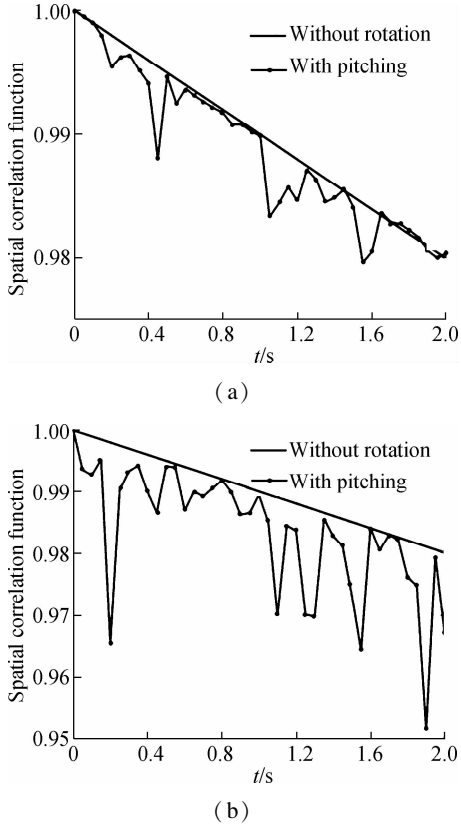

Fig. 6 Space correlation functions with rotation. (a) Pitching operations; (b) Rolling operation

Fig. 7 depicts the Doppler power spectral density of the DB components under various UAV displacements. The Doppler power spectral density is higher near the maximum Doppler frequency when the UAV moves toward or directly away from the scattering-concentrated region surrounding it, as depicted in the figure. Furthermore, the power spectral density curve is narrow. The Doppler power spectrum becomes widely dispersed when the UAV moves in other directions. According to the simulation results, the shape of the Doppler power spectral density depends on the relationship between the scatterer distribution and the UAV's displacement.

4 Conclusions

1) This paper proposes a novel two-cylinder-based 3D GBSM for UAV non-stationary A2G MIMO channels. The proposed model considers the UAV's rotations and accelerated motions, displacing the channel and making it non-stationary.

2) Following this, the computational methods for UAV antenna array angles and time-variant parameters, such as propagation time delays and maximum Doppler frequencies, are derived. The channel space-time correlation functions are derived from previous results.

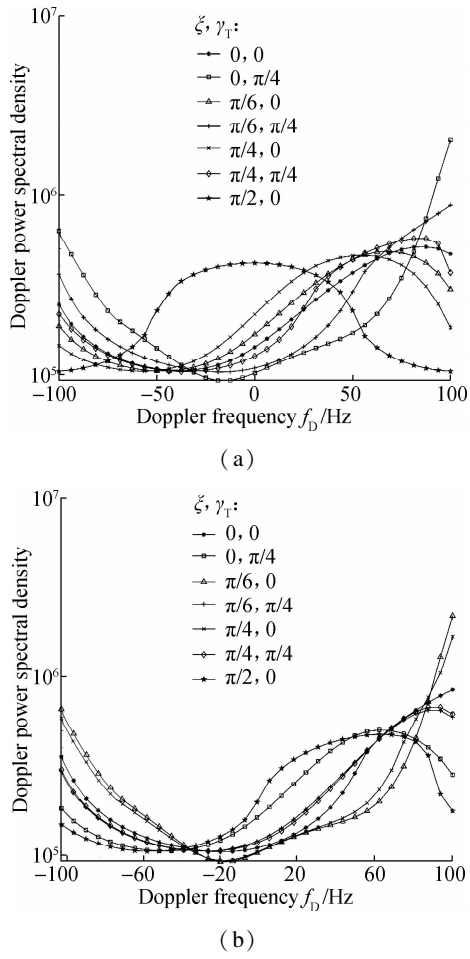

Fig. 7 Doppler power spectral density under different directions. (a) $\beta_0 = \pi/6$; (b) $\beta_0 = \pi/3$

3) Finally, numerical simulations are executed to validate the statistical properties of the channel. The simulation results indicate that the channel exhibits higher stationarity in the time domain when the UAV moves along the LoS direction. With increasing UAV and GS accelerations, the time correlation function becomes smaller at the same time delay, indicating an increase in the time domain non-stationarity of the channel. The UAV's rotation significantly affects the spatial correlation function, with rolling having a greater effect than pitching.

References

[1] Mozaffari M, Saad W, Bennis M, et al. A tutorial on UAVs for wireless networks: Applications, challenges, and open problems[J]. *IEEE Communications Surveys & Tutorials*, 2019, **21**(3): 2334 - 2360. DOI: 10.1109/COMST.2019.2902862.

[2] Duo B, Li Y L, Hu H, et al. Joint robust 3D trajectory and communication design for dual-UAV enabled secure communications in probabilistic LoS channel[J]. *Ad Hoc Networks*, 2021, **121**: 102592. DOI: 10.1016/j.adhoc.2021.102592.

[3] Yan C X, Fu L G, Zhang J K, et al. A comprehensive survey on UAV communication channel modeling[J]. *IEEE Access*, 2019, **7**: 107769 - 107792. DOI: 10.

1109/ACCESS. 2019. 2933173.
[4] Khawaja W, Guvenc I, Matolak D W, et al. A survey of air-to-ground propagation channel modeling for unmanned aerial vehicles[J]. *IEEE Communications Surveys & Tutorials*, 2019, **21**(3): 2361 - 2391. DOI: 10. 1109/COMST. 2019. 2915069.
[5] Gao Z B, Liu B, Cheng Z P, et al. Marine mobile wireless channel modeling based on improved spatial partitioning ray tracing[J]. *China Communications*, 2020, **17**(3): 1 - 11. DOI: 10. 23919/JCC. 2020. 03. 001.
[6] Zaman M A, Mamun S A, Gaffar M, et al. Modeling VHF air-to-ground multipath propagation channel and analyzing channel characteristics and BER performance [C]//2010 *IEEE Region* 8 *International Conference on Computational Technologies in Electrical and Electronics Engineering*. Irkutsk, Russia, 2010: 335 - 338. DOI: 10. 1109/SIBIRCON. 2010. 5555104.
[7] Jia R B, Li Y R, Cheng X, et al. 3D geometry-based UAV-MIMO channel modeling and simulation[J]. *China Communications*, 2018, **15**(12): 64 - 74. DOI: 10. 12676/j. cc. 2018. 12. 005.
[8] Jiang H, Zhang Z C, Gui G. Three-dimensional non-stationary wideband geometry-based UAV channel model for A2G communication environments[J]. *IEEE Access*, 2019, **7**: 26116 - 26122. DOI: 10. 1109/ACCESS. 2019. 2897431.
[9] Zeng L Z, Cheng X, Wang C X, et al. A 3D geometry-based stochastic channel model for UAV-MIMO channels [C]//2017 *IEEE Wireless Communications and Networking Conference*. San Francisco, CA, USA, 2017: 1 - 5. DOI: 10. 1109/WCNC. 2017. 7925794.
[10] Chang H T, Bian J, Wang C X, et al. A 3D non-stationary wideband GBSM for low-altitude UAV-to-ground V2V MIMO channels[J]. *IEEE Access*, 2019, **7**: 70719 - 70732. DOI: 10. 1109/ACCESS. 2019. 2919790.
[11] Bian J, Wang C X, Liu Y, et al. 3D non-stationary wideband UAV-to-ground MIMO channel models based on aeronautic random mobility model[J]. *IEEE Transactions on Vehicular Technology*, 2021, **70**(11): 11154 - 11168. DOI: 10. 1109/TVT. 2021. 3116953.
[12] Chang H T, Wang C X, Liu Y, et al. A novel nonstationary 6G UAV-to-ground wireless channel model with 3-D arbitrary trajectory changes[J]. *IEEE Internet of Things Journal*, 2021, **8**(12): 9865 - 9877. DOI: 10. 1109/JIOT. 2020. 3018479.
[13] Jiang H, Zhang Z C, Wang C X, et al. A novel 3D UAV channel model for A2G communication environments using AoD and AoA estimation algorithms[J]. *IEEE Transactions on Communications*, 2020, **68**(11): 7232 - 7246. DOI: 10. 1109/TCOMM. 2020. 3011716.
[14] Ma Z F, Ai B, He R S, et al. Impact of UAV rotation on MIMO channel characterization for air-to-ground communication systems[J]. *IEEE Transactions on Vehicular Technology*, 2020, **69**(11): 12418 - 12431. DOI: 10. 1109/TVT. 2020. 3028301.
[15] Cheng X, Li Y R, Wang C X, et al. A 3-D geometry-based stochastic model for unmanned aerial vehicle MIMO ricean fading channels[J]. *IEEE Internet of Things Journal*, 2020, **7**(9): 8674 - 8687. DOI: 10. 1109/JIOT. 2020. 2995707.
[16] Zeng L Z, Cheng X, Wang C X, et al. Second order statistics of non-isotropic UAV ricean fading channels[C]// 2017 *IEEE* 86*th Vehicular Technology Conference*. Toronto, ON, Canada, 2017: 1 - 5. DOI: 10. 1109/VTCFall. 2017. 8287893.
[17] Zhang X, Cheng X. Second order statistics of simulation models for UAV-MIMO ricean fading channels[C]// 2019 *IEEE International Conference on Communications*. Shanghai, China, 2019: 1 - 6. DOI: 10. 1109/ICC. 2019. 8761565.
[18] Ma Z F, Ai B, He R S, et al. A wideband non-stationary air-to-air channel model for UAV communications[J]. *IEEE Transactions on Vehicular Technology*, 2020, **69**(2): 1214 - 1226. DOI: 10. 1109/TVT. 2019. 2961178.

一种无人机空地 MIMO 信道的三维几何随机模型

燕 锋[1,2] 周天香[1] 李 昊[2] 庞井明[3] 丁 凯[2] 夏玮玮[1] 沈连丰[1]

([1] 东南大学移动通信国家重点实验室, 南京 210096)
([2] 近地面探测技术重点实验室, 无锡 214035)
([3] 江苏中利电子信息科技有限公司, 常熟 215542)

摘要:提出一种针对无人机空地多输入多输出信道的三维非平稳几何随机模型. 模型中无人机侧和地面站侧的散射体分别分布在两侧的 2 个圆柱体表面. 为描述信道的非平稳性,所提模型考虑了无人机的旋转和加速度的影响. 从理论上推导了对应时变参数的计算方法,包括无人机天线阵列角度、时延和最大多普勒频率. 在此基础上,进一步推导了信道空时相关函数和多普勒功率谱密度等统计特性. 最后,通过数值仿真验证了信道的统计特性. 仿真结果表明:无人机和地面站的加速度越大,时间相关函数的值越小,信道在时域上的非平稳性越大;无人机旋转对空间相关性有重要影响,滚转运动对空间相关性的影响比俯仰运动更显著;无人机运动方向对多普勒功率谱密度有显著影响.

关键词:无人机; 几何随机模型; 空地信道
中图分类号:TN929